Available online at www.CivileJournal.org

Civil Engineering Journal

(E-ISSN: 2476-3055; ISSN: 2676-6957)

Vol. 12, No. 03, March, 2026

A Preliminary Study of the Mechanical Performance of a Novel FBG-Based Flexible Stress Sensor

Gang Bi [1*], Long Yang [1], Fan Li [1]

[1] College of Transportation Science and Engineering, Nanjing Tech University, Nanjing 210009, China.

Received 26 September 2025; Revised 12 February 2026; Accepted 16 February 2026; Published 01 March 2026

Abstract

Soil stress monitoring is critical for accurate soil state assessment in geotechnical engineering, yet conventional resistance-based stress sensors—typically encapsulated in rigid materials—often generate measured values deviating upward from analytical solution predictions, limiting their practical reliability. To address this key limitation, this study aims to propose a novel fiber Bragg grating (FBG)-based flexible stress sensor that integrates the high precision of FBG technology with the adaptive conformability of flexible sensing platforms. For validation, systematic physical modeling tests were conducted using multiple soil types (clay and sand) under different loading protocols, where the proposed sensor's performance was comprehensively compared with that of a conventional resistance-based rigid sensor. Key findings reveal that the FBG-based flexible sensor delivers more accurate stress measurements in both clay and sand; notably, during cyclic loading within the elastic range, it reverts to its initial state with minimal hysteresis, outperforming the rigid counterpart in dynamic stability. The novelty of this work lies in the fusion of FBG sensing with flexible encapsulation, which mitigates the overestimation issue of rigid sensors and enables more reliable soil stress monitoring for geotechnical applications.

Keywords: Flexible Stress Sensor; FBG; Physical Modeling; Sensor Design; Sensor Testing.

1. Introduction

Accurate in-situ soil stress measurement is fundamental to assessing geotechnical stability and deformation, which are critical for the safety and design of civil infrastructure [1]. Traditional analytical and numerical methods for stress prediction—ranging from limit equilibrium analyses to advanced finite element simulations—are inherently constrained by idealized assumptions regarding material homogeneity and boundary conditions [2]. Consequently, they often fail to accurately capture the complex, heterogeneous stress fields in real engineering settings, leading to potential discrepancies between predicted and actual soil behavior [3]. Consequently, direct field monitoring remains indispensable for obtaining reliable stress data.

The advent of fiber optic sensing, particularly Fiber Bragg Grating (FBG) technology, has introduced new possibilities for geotechnical instrumentation due to its high precision, electromagnetic immunity, and long-term stability [4-6]. To overcome the low-pressure sensitivity of bare FBGs, encapsulation techniques have been widely adopted [7-9]. Additive manufacturing has become an established and efficient method for sensor packaging in recent years [10-13]. However, most encapsulation materials—whether for conventional electrical sensors or FBG-based ones—are rigid, causing stiffness mismatch with the surrounding soil matrix. This leads to significant measurement inaccuracies known as "matching errors", which distort the actual stress field [14-17]. To minimize this error, it is essential for the mechanical

* Corresponding author: gbi@njtech.edu.cn

https://doi.org/10.28991/CEJ-2026-012-03-010

properties (especially stiffness) of the encapsulation material to match those of the surrounding geo-materials. Flexible pressure sensors, designed with compliant materials, represent a promising approach to achieving this mechanical compatibility.

Although similar flexible pressure sensors have gained considerable attention in robotics and biomedical fields [18-20], their integration with FBG technology for geotechnical stress sensing remains notably underdeveloped. Recent studies on FBG-based flexible sensors focus primarily on tactile perception, medical devices, or structural surface monitoring [21-23], with limited investigation into soil-stress interaction under confined, high-pressure conditions. Therefore, a critical gap exists in the development of a flexible, FBG-based stress sensor specifically designed for accurate, minimally intrusive soil stress measurement.

To address this gap, this study proposes a novel FBG-based flexible stress sensor that synergizes the high sensitivity and durability of FBG with the soil-conforming capability of flexible encapsulation. The sensor was designed, fabricated via additive manufacturing, and systematically evaluated through laboratory calibration and physical modeling tests in various soil media under different loading conditions. This research aims to validate whether the flexible design can reduce stiffness mismatch errors and provide more accurate stress measurements compared to conventional rigid sensors.

The article proceeds as follows. Beginning with the working principle of the flexible FBG stress sensor in Section 2. Section 3 then details how the sensor was designed and fabricated, including its encapsulation. Following this, Section 4 reports the calibration procedure and results. Section 5 presents and discusses the experimental outcomes from physical modeling tests under various loading conditions. The paper concludes in Section 6 with a summary of findings and recommendations for future work.

2. Theoretical Approach

As shown in Figure 1, the working principle of the FBG is based on measuring shifts in the center wavelength of reflected light to detect external physical variations. In general, it is described by the following equation:

$$\lambda = 2\Lambda n_e \tag{1}$$

where λ is the center wavelength of the FBG, n_e is the effective refractive index of the fiber, and Λ is the grating period.

The shift of the center wavelength induced by external physical variations can be derived as follows:

$$\Delta\lambda = 2(\Delta\Lambda)n_e + 2\Lambda(\Delta n_e) \tag{2}$$

where $\Delta\lambda$ is the shift of the center wavelength of the FBG, Δn_e is the change of the effective refractive index of the fiber, and $\Delta\Lambda$ is the change of the grating period. Meanwhile, according to the Brillouin scattering theory, it has,

$$\frac{\Delta\lambda}{\lambda} = (1 - C)\Delta\varepsilon \tag{3}$$

where C is the valid elastic-optic constant of the FBG, and $\Delta\varepsilon$ is the axial strain of the FBG.

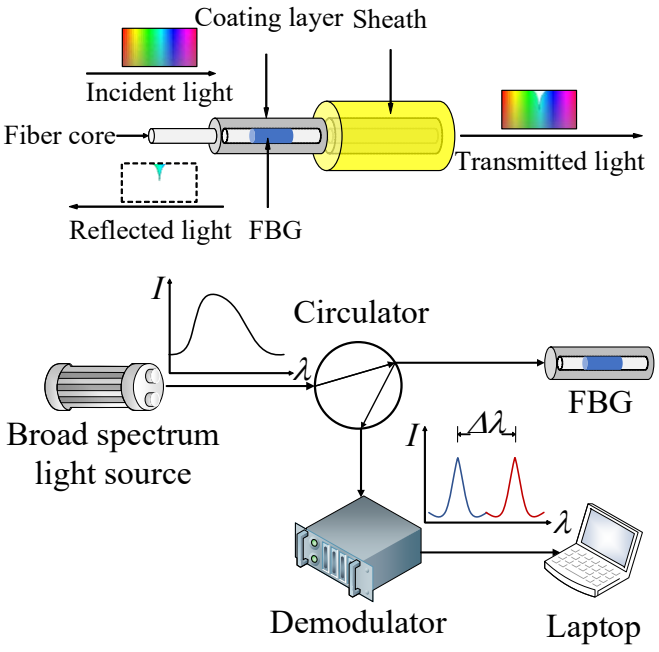

Figure 1. The working principle of the FBG

When the FBG is encapsulated with flexible materials, the axial strain induced by external pressure is,

$$\Delta\varepsilon = -\frac{\Delta P(1-2\upsilon)}{E} \quad (4)$$

where, ΔP is the stress, υ is the Poisson's Ratio of flexible materials, and E is Young's Modulus of flexible materials.

By combining Equation 3 and Equation 4, and taking into account the stress loss during the transmission, it can derived that,

$$\frac{\Delta\lambda}{\lambda} = \eta K_p \Delta P \quad (5)$$

where, η is the transmission coefficient of the flexible material, and K_p is the pressure sensitivity of the FBG, which has,

$$K_p = -\frac{(1-C)(1-2\upsilon)}{E} \quad (6)$$

3. Design

3.1. Encapsulation Material

In this study, an embedded encapsulation method was adopted for the FBG-based soil stress sensor, while a conventional resistance strain gauge-based sensor served as the benchmark for comparison. The bare FBG, with an outer diameter of approximately 100 μm (Table 1), is mechanically fragile and possesses low intrinsic pressure sensitivity. Consequently, encapsulation is essential both to provide mechanical protection against breakage and to enhance its pressure response.

Table 1. Parameters of the FBG

Parameter type (unit)	Parameter value
Central wavelength (nm)	1520-1565
Bandwidth (nm)	0.217
Side mode suppression ratio (dB)	15
Grid length (mm)	10
Stripping length (mm)	12-15
Reflectance (%)	92-93
Tail length (m)	2+2

The encapsulation design must fulfill two primary requirements: structural simplicity to prevent fiber damage, and efficient strain transfer to the sensing core. Therefore, a polymer was selected as the encapsulation material to ensure the encapsulated sensor's elastic modulus remains significantly lower than that of the surrounding soil. Specifically, a silicone gel solution ($xSiO_2 \cdot yH_2O$) was chosen (Table 2) owing to its favorable mechanical properties, biocompatibility (eco-friendly, non-toxic), and safety (non-irritating, non-allergenic).

Table 2. Parameters of the silica gel solution

Performance indicator (unit)	Silica gel solution
Composition	$xSiO_2 \bullet yH_2O$
Appearance	Milky liquid
Shore hardness (A)	5
Extension strength (psi)	315
Curing temperature (℃)	25~150
Temperature resistance (℃)	-45~200

3.2. Structural Design

The proposed FBG-based flexible stress sensor features a "cross-shaped" sensing unit. This design addresses the fact that FBGs are sensitive primarily to axial strain by orienting the gratings to effectively perceive stress. Two FBGs are arranged within the unit to compensate for potential loading eccentricity through averaging their wavelength shifts. The sensing unit is centrally embedded 5 mm deep within a cylindrical flexible matrix (silicone encapsulation, Ø40 mm × 10 mm), aligned parallel to its base. Under applied stress, the matrix deformation induces axial strain in the FBGs. The resulting wavelength shift is then measured to calculate the strain and, consequently, infer the applied stress.

3.3. Encapsulation Process

The encapsulation process is shown in Figure 2.

- Mold Fabrication: The encapsulation mold was designed in SolidWorks and fabricated using a 3D printer. It consists of upper and lower chambers, with a side slot for fiber fixation and a top opening in the upper chamber for resin infusion. Prior to use, the mold surfaces and internal cavities were cleaned with lint-free paper soaked in anhydrous alcohol. Subsequently, a thin layer of Vaseline was evenly applied to all internal surfaces, including perforations and partition gaps, to serve as a release agent for demolding.
- FBG Preparation: Prior to encapsulation, the non-sensing section of the optical fiber was sleeved and secured. This protection was implemented to prevent fiber displacement or detachment during the demolding process and subsequent mechanical testing.
- Silicone Encapsulant Preparation: The silicone encapsulant was prepared by mixing the base solution with the curing agent at a weight ratio of 100:3. Subsequently, the mixture was stirred at a constant speed using a glass rod until a homogeneous, bubble-free state was achieved.
- Sensor Encapsulation: The prepared silicone mixture was first poured slowly into the 3D-printed mold until it reached half-height. Subsequently, the pre-processed FBG was carefully positioned into the axial slot of the mold. A slight pre-stress was applied to the fiber to maintain its alignment. Following this, the remaining silicone was poured to fill the mold completely. The entire pouring process was completed within 10 minutes to prevent premature curing from exothermic reaction. Finally, the assembly was cured at room temperature for 8 hours to solidify.
- Sensor Demolding: Upon complete curing of the silicone, the sensor was carefully demolded. This process involved first removing the upper mold chamber and then gently extracting the solidified sensor. The demolded sensor was inspected for integrity and to ensure the FBG fiber remained properly aligned and undamaged.
- Fiber Functionality Check: The embedded optical fiber was tested after demolding and confirmed to be fully operational, indicating no damage occurred during the encapsulation and demolding processes.

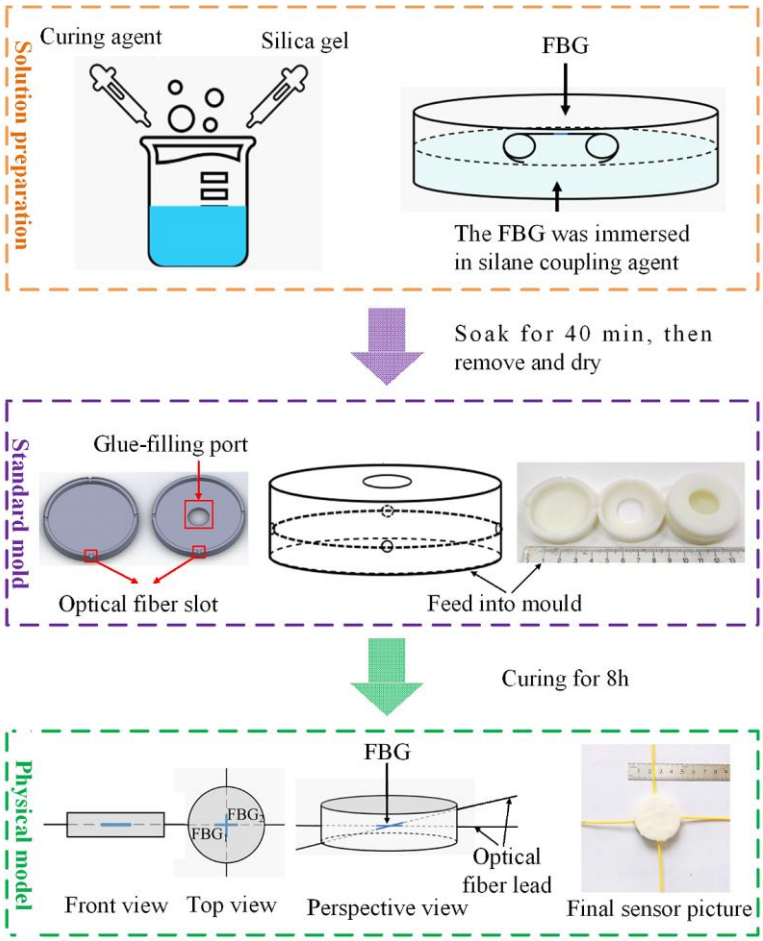

Figure 2. The encapsulation of the proposed sensor

4. Calibration

4.1. Calibration Setup

Calibration Procedure: The calibration setup is depicted in Figure 3. Prior to formal calibration, three preliminary loading-unloading cycles were applied to eliminate any residual prestress in the sensor. Subsequently, a five-level stepwise loading-unloading test was conducted using calibrated masses. At each load level, data were acquired at 1 Hz for 60 seconds after pressure stabilization. To mitigate random errors, the entire loading-unloading procedure was repeated three times. The mean shift of the two central wavelengths was calculated for each load step across all replicates. Finally, a linear regression was performed between the average wavelength shift and the applied load to establish the sensor's calibration curve.

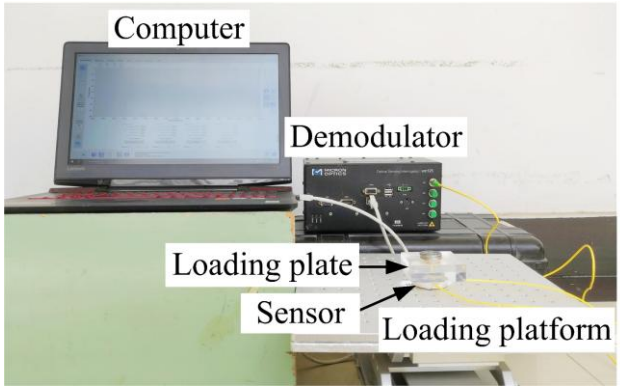

Figure 3. The setup of the calibration

4.2. Calibration Results

Following the procedures in Section 3, four sensors (S1-S4) of two types were fabricated. Specifically, sensors S3 and S4 underwent an additional step where the FBG was immersed in a silane coupling agent during fabrication. The performance of these sensors was evaluated through calibration (Figure 4) and quantified using four indicators, as presented in Tables 3 through 5.

The first one is the hysteresis e_H, as defined:

$$e_H = \pm \frac{\Delta H_{max}}{y_{FS}} \times 100\% \tag{7}$$

where, ΔH_{max} is the maximum deviation of the output in the positive and negative strokes, and y_{FS} is the full-scale output value.

The second one is the repetitive error, as defined:

$$e_R = \pm \frac{\alpha \sigma_{max}}{y_{FS}} \times 100\% \tag{8}$$

where, σ_{max} is the maximum value of the standard deviation of the output values in the positive and negative strokes, and α is 3 corresponding to the confidence probability of 99.73%.

The third indicator, known as linearity, is defined as:

$$e_H = \pm \frac{\Delta_{max}}{y_{FS}} \times 100\% \tag{9}$$

where, Δ_{max} is the maximum deviation between the output average value and the fitting line.

The fourth indicator sensitivity refers to the ratio of the output quantity increment of the sensor in the stable state Δy to the input quantity increment measured Δx.

$$s = \frac{\Delta y}{\Delta x} \tag{10}$$

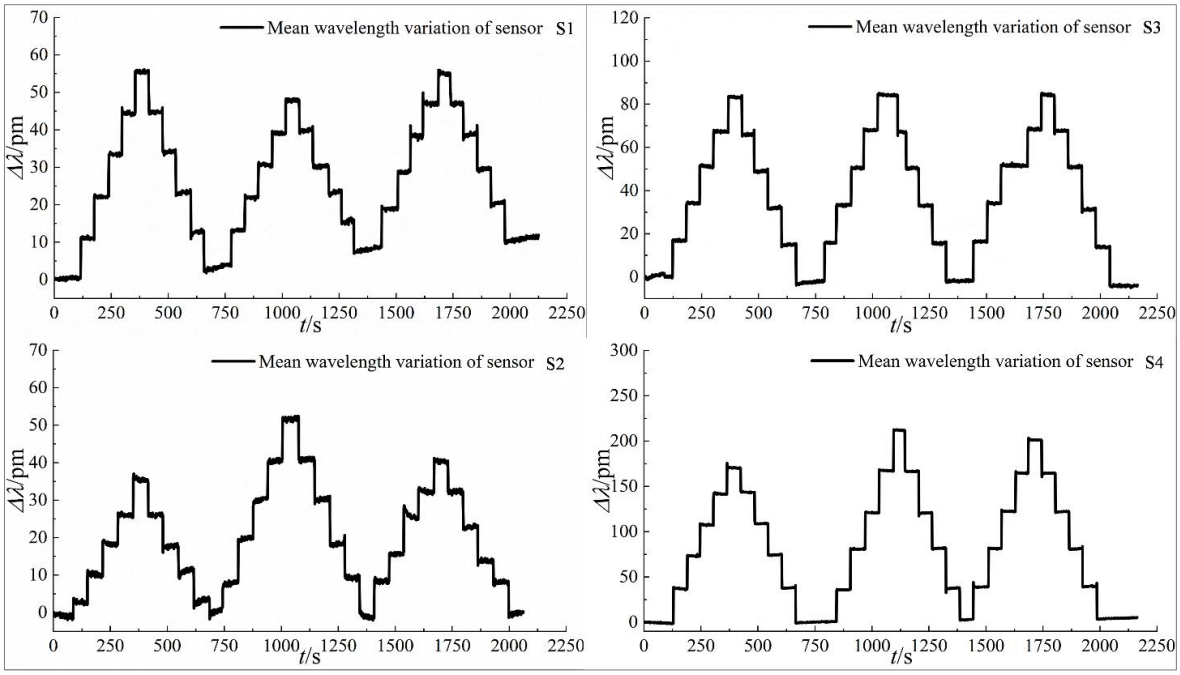

Figure 4. Time history diagram of the average wavelength changes of the sensor

Table 3. The hysteresis of the sensor

Sensor	S1	S2	S3	S4
ΔH_{max} (pm)	1.689	0.853	2.703	1.81
	2.295	2.412	0.941	1.99
	1.504	0.650	3.238	0.495
e_H (%)	5.12	3.68	3.75	1.06

Table 4. The repeatability error of the sensor

Sensor No.	Positive stroke repeatability error (%)	Reverse stroke repeatability error (%)	Mean repeatability error (%)
S1	12.48	12.36	12.42
S2	12.28	13.94	13.11
S3	2.33	3.66	3.00
S4	9.98	9.84	9.91

Table 5. Sensor calibration test fits the curve expression

Sensor	Linearity R^2	Sensitivity (pm/Pa)
S1	0.99	0.072
S2	0.99	0.075
S3	0.99	0.123
S4	0.99	0.100

Figure 5. presents the fitted calibration curves (average wavelength shift vs. load) for all sensors across three loading cycles. The data consistently show that sensors treated with a silane coupling agent (S3, S4) exhibit higher sensitivity than their untreated counterparts (S1, S2). This enhancement is attributed to improved adhesion at the FBG-silicone interface, thus facilitating more accurate load transfer and consequently higher sensitivity. Based on these results, the S4 sensor was selected for subsequent physical modeling tests.

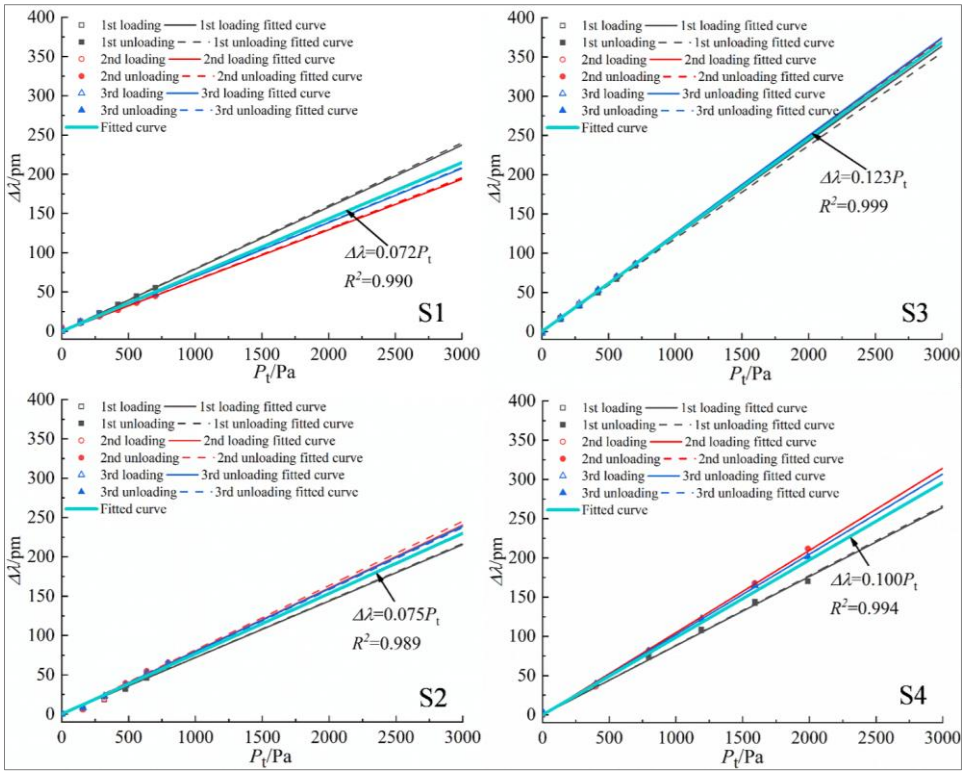

Figure 5. Fitting curves of the calibration

5. Test

To benchmark its performance, the proposed FBG-based flexible stress sensor was evaluated alongside a conventional resistance-based sensor, hereafter referred to as the rigid sensor.

5.1. Properties

Two soil media from Nanjing, China—red clay and fine sand—were used, with their key properties provided in Table 6.

Table 6. Soil properties

Soil	Unit weight (kN/m³)	Moisture content (%)	Cohesion (kPa)	Friction Angle (°)	Young's Modulus (MPa)
Red clay	18.5	2.1	34.90	4.21	3.8
Fine sand	14.5	3.0	0.75	31.70	5.5

The modulus E of the proposed sensor is obtained using Equation 11 [24],

$$E = \frac{P(1-\nu^2)}{2a\omega\kappa} \tag{11}$$

where, P is the contact force, υ is the Poisson's Ratio of flexible materials (i.e., silicone), which is taken as 0.48 as usual [25], a is the radius of the cylindrical indenter, ω is the indentation depth, and κ is the correction factor.

Sensor Elastic Modulus Test: A cylindrical indenter (radius = 5 mm) was fabricated and positioned on the sensor's upper surface. The loading head of the universal testing machine was then lowered onto the indenter to establish firm contact. The test was conducted at a constant displacement rate of 1 mm/min for a total duration of 7 minutes. The contact force was recorded at the target indentation depth of 1.5 mm. Following three replicate tests, the elastic modulus of the sensor was calculated using Equation 11 (Table 7).

Table 7. The elastic modulus of the proposed sensor

ω/h	κ	*P*/N	*E*/MPa	$\bar{E}$/MPa
15%	2.269	5.514	0.122	0.108
		4.983	0.110	
		4.227	0.093	

5.2. Setup

A cubic model box with internal dimensions of 50 cm × 50 cm × 50 cm (L×W×H) was employed for the physical modeling tests (Figure 6.). The box was constructed with a stainless-steel frame and transparent acrylic sidewalls, to allow for visual observation of the internal soil conditions. The box was backfilled with soil to a height of 25 cm. A loading plate measuring 6 cm × 6 cm × 1.5 cm was then positioned at the center of the soil surface. The sensor was buried 5 cm directly beneath the center of the loading plate.

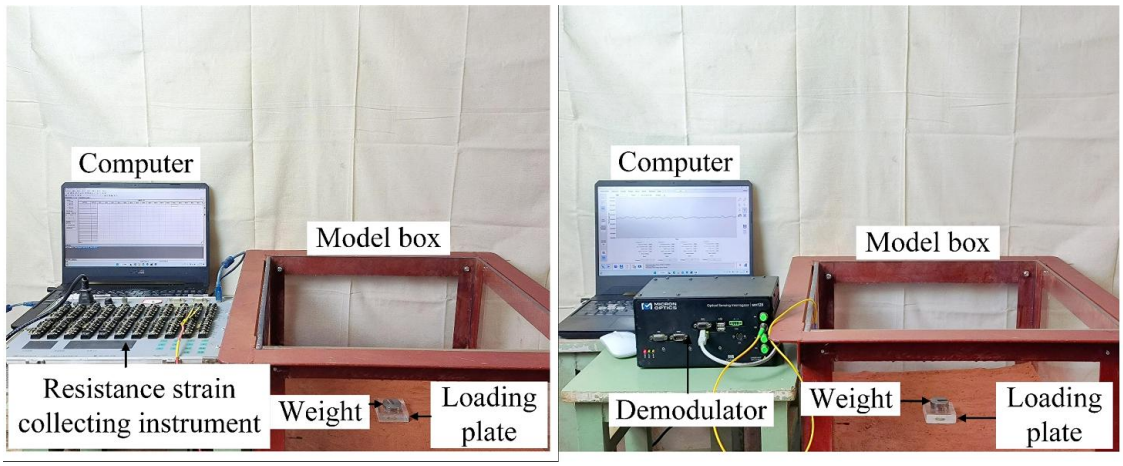

Figure 6. The setup of the test for two types of sensors

The stratified backfilling procedure (Figure 7) commenced with applying Vaseline to the model box sidewalls to reduce boundary friction. Following this, a baseline was marked on the acrylic walls to guide the placement of 5-cm-thick soil layers. Each layer was compacted with a vibratory compactor and its surface was then scarified to improve interlayer coupling. After backfilling to a depth of 20 cm, the sensor was installed at the center, with its connecting wires carefully routed along the sidewalls. Subsequently, backfilling continued with careful compaction using a pressure plate until the sensor reached a burial depth of 5 cm. The completed model was then allowed to rest for 24 hours to achieve initial stress equilibrium.

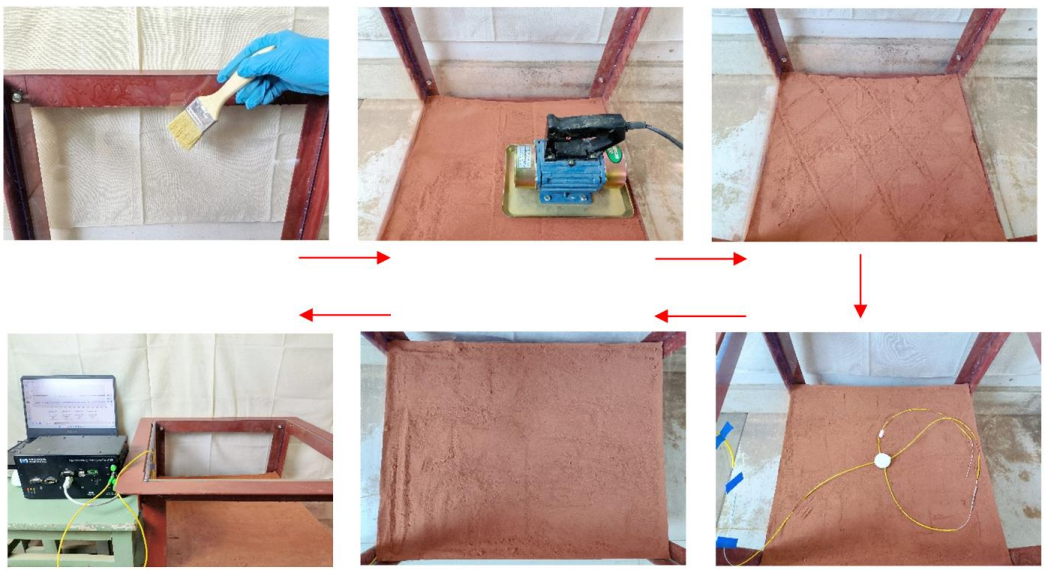

Figure 7. The setup of the modeling box

After the rest period, the instruments were connected and the initial data were verified for stability. The data acquisition system was synchronized and initiated at a 1 Hz sampling rate, with the initial FBG wavelength recorded. A loading plate was then centered on the soil surface. Loading began with standardized weights after sensor readings stabilized. A three-level cyclic test was conducted: before any weight change, data stability was confirmed; once stable, the average FBG response was recorded for that load level. After unloading, the next cycle commenced upon data re-stabilization. This process was repeated for three full cycles. Subsequently, cyclic tests with five, six, and seven load levels were performed under identical conditions, following the protocol in Table 8.

Table 8. Loading protocols

Soil	Overburden single weight/g	Overburden single stage load/Pa	Loading levels	Maximum overlying load/Pa	Case
Red clay	18	143.24	3	429.7	A-1
			5	716.2	A-2
			7	1002.7	A-3
	50	397.89	3	1193.7	A-4
			5	1989.5	A-5
			6	2387.3	A-6
Fine sand	50	397.89	3	1193.7	B-1
			5	1989.5	B-2
			6	2387.3	B-3

5.3. Results and Discussion

This section presents a comprehensive comparative analysis of the resistance-based rigid sensor and the proposed FBG-based flexible sensor across different soil media. The stress measured by both types of sensors is plotted against the theoretical stress in this study. The abscissa is the theoretical value of the additional stress of soil is given by the Bousinesq solution:

$$\sigma_0 = K_c P_0 \tag{12}$$

where, P_0 is the applied pressure, K_c is the coefficient with the value of 0.142 herein, and σ_0 is the targeted measured stress by sensors.

The ordinate either for the resistance-based rigid stress sensor, the measured stress:

$$\sigma_{tr} = K_r \varepsilon \tag{13}$$

where, ε is the microstrain, K_r is the coefficient with a value of 39.53 after the calibration, and σ_{tr} is the measured stress by the resistance-based rigid sensor.

The ordinate or for the FBG-based flexible stress sensor, the measured stress:

$$\sigma_{tf} = K_f \Delta\lambda \tag{14}$$

where, $\Delta\lambda$ is the shift of the center wavelength of the FBG, K_f is the coefficient with the value of 10.0 ("S4" in Table 5), and σ_{tf} is the measured stress by the FBG-based flexible sensor.

Figures 8 to 11 provide critical insights into measurement accuracy, stability, and sensor-soil interaction. As clearly depicted in Figures 8 and 9, a consistent and significant trend is observed: the stress measured by the rigid sensor is systematically higher than the theoretical Boussinesq solution, while the stress measured by the flexible sensor is systematically lower. This symmetrical deviation pattern is not random but is a direct manifestation of stress perturbation caused by stiffness mismatch at the sensor-soil interface. The rigid sensor, with an elastic modulus order of magnitude greater than the soil, acts as a stiff inclusion. This creates an arching effect in the surrounding soil matrix, amplifying the normal stress on its sensing surface and leading to overestimation [4, 13, 17]. Conversely, the proposed flexible sensor is encapsulated in silicone, the modulus of which was deliberately selected to be on the same order of magnitude as the soil. This compliance allows the sensor to deform conjointly with the soil, minimizing stress concentration. However, as the encapsulation material still possesses finite stiffness, it provides slight support to the surrounding soil, which may result in a measured stress marginally below the ideal theoretical value. This bidirectional deviation conclusively proves that stiffness compatibility is the fundamental factor governing measurement fidelity. The closer agreement of the flexible sensor's data with the theoretical solution demonstrates the efficacy of the compliant design in mitigating interfacial stress disturbance.

A comparison between Figure 8. (red clay) and Figure 9. (fine sand) reveals a pronounced dependency of sensor performance on soil type. In cohesive red clay, data from both sensors show relatively low scatter, indicated by high coefficients of determination (R^2) for their fitting curves. This is likely due to the plastic nature of clay, which facilitates more continuous and uniform stress redistribution around the sensor. In contrast, the performance disparity widens dramatically in granular fine sand. The data from the rigid sensor exhibit significantly increased scatter (lower R^2), while the flexible sensor maintains exceptional stability (R^2 remains near 0.99). This phenomenon highlights the inherent instability of rigid sensors in granular materials. Stress transmission in sand occurs through a network of force chains via particle contacts. The intrusion of a rigid sensor severely disrupts this network, creating a highly heterogeneous and load-path-dependent local stress state, which yields volatile signals. The compliant flexible sensor, by minimizing this disruption and integrating more seamlessly into the soil fabric, achieves stable and repeatable measurements. This finding underscores a key advantage of the flexible design for monitoring discontinuous, granular media.

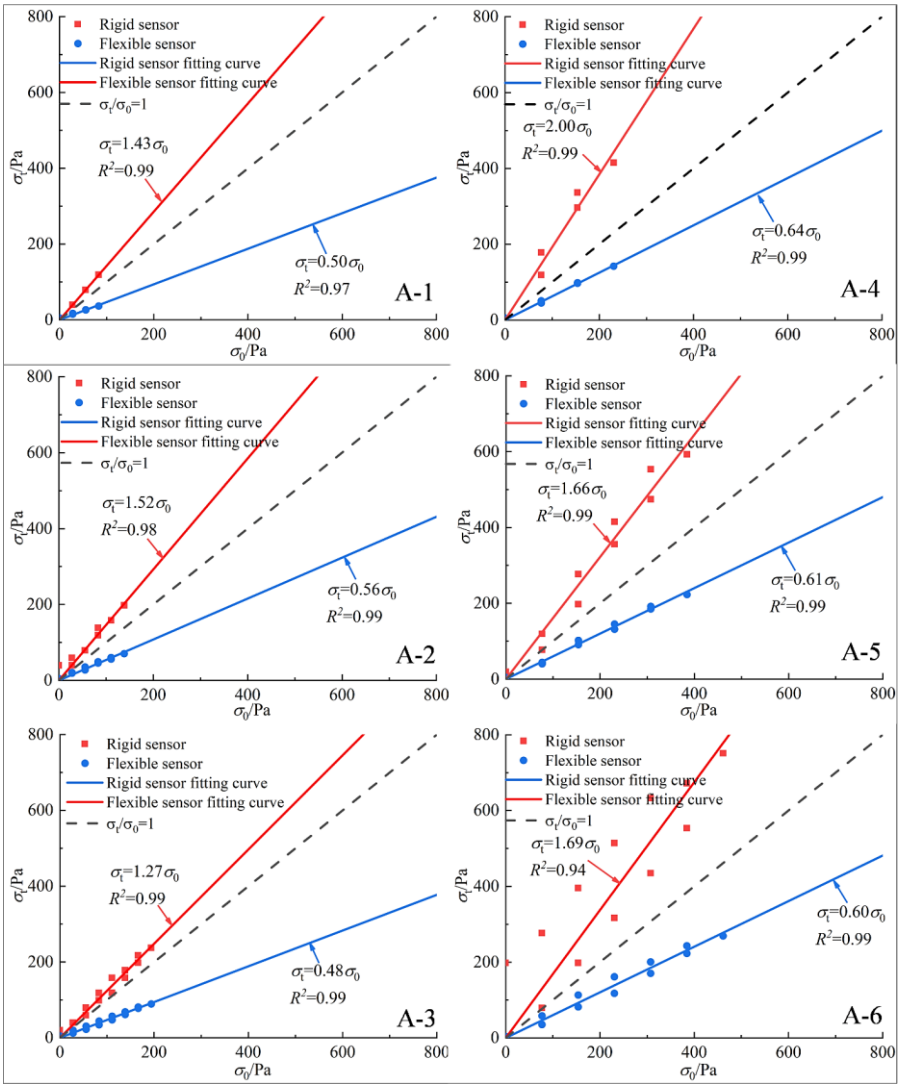

Figure 8. Comparison of two sensors in red clay

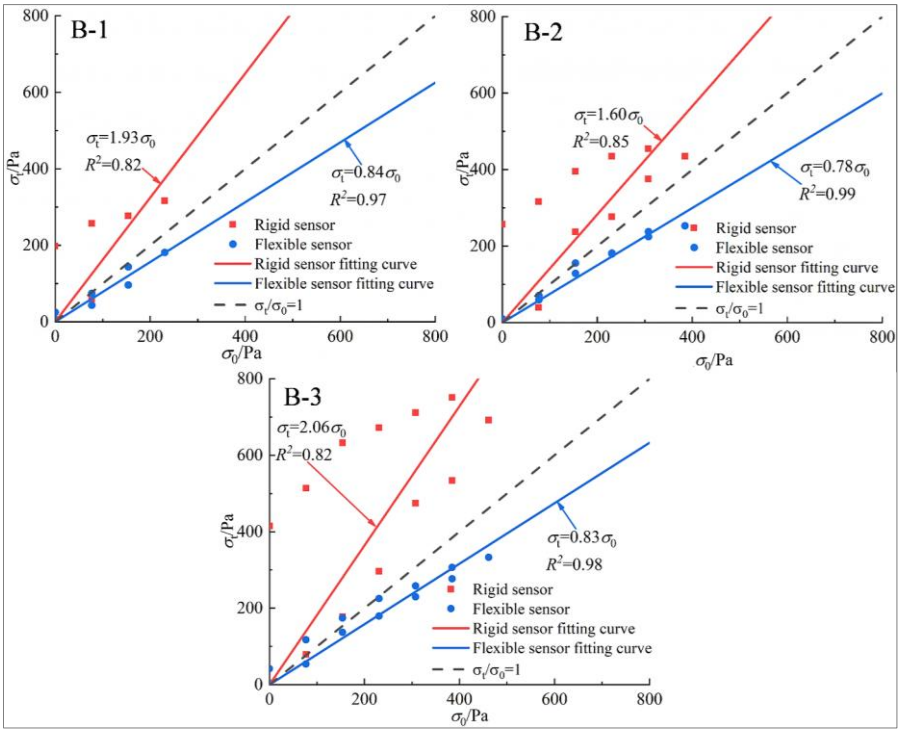

Figure 9. Comparison of two sensors in fine sand

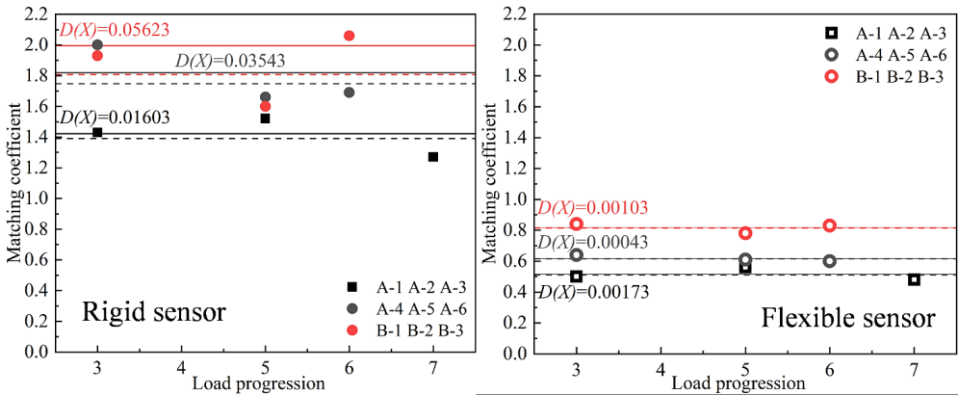

Figure 10. The variance of the matching coefficient of two sensors

Figure 10 provides a dynamic perspective by plotting the variance of the "matching coefficient" (measured stress / theoretical stress) throughout the loading progression. The curve for the flexible sensor shows narrower fluctuation bands around a mean value slightly below 1.0, remaining stable across all load levels. This visually confirms its measurement consistency and reliability. In stark contrast, the rigid sensor's matching coefficient not only averages significantly above 1.0 but also exhibits large, erratic fluctuations, with a variance substantially higher than that of the flexible sensor. This high variance indicates that the error for the rigid sensor is not a consistent offset but an unstable variable influenced by loading history. Each load cycle likely alters the contact conditions and arching geometry around the rigid inclusion, causing sensitivity drift. The stable matching coefficient of the flexible sensor suggests its measurement mechanism is less susceptible to such hysteretic effects, pointing to superior potential for long-term stability.

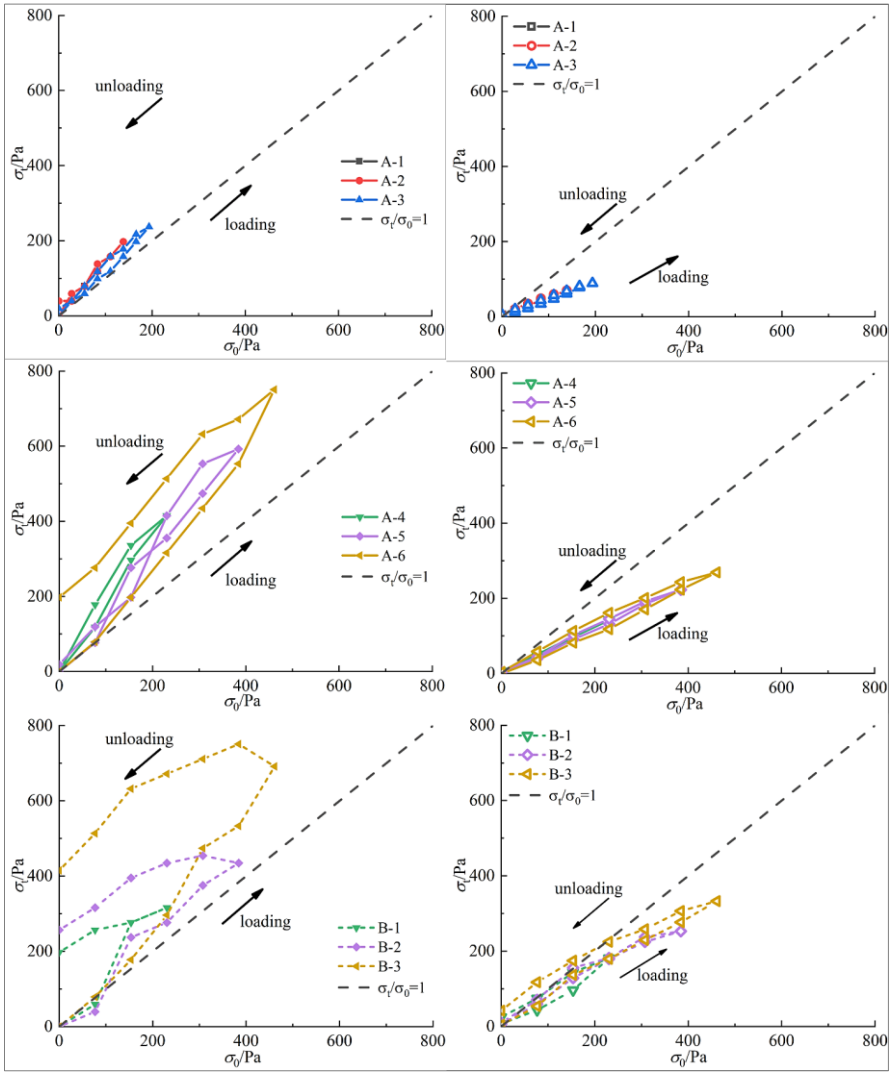

Figure 11. Hysteresis curves: rigid sensor (left) and flexible sensor (right)

The hysteresis curves in Figure 11 offer crucial insight into the sensors' mechanical behavior. The loading and unloading paths for the rigid sensor are distinctly separated, forming a significant hysteresis loop, and the unloading path fails to return to the origin. This indicates the occurrence of irrecoverable plastic deformation or slippage, either within the sensor-soil interface or in the adjacent soil itself. Energy is dissipated in this process, rendering the sensor incapable of accurately tracking stress removal—a critical drawback for monitoring unloading or cyclic events (e.g., excavations, earthquakes). Conversely, the hysteresis loop for the flexible sensor is nearly negligible. Its unloading path closely follows the loading path back to the origin, demonstrating that the sensor operates in a highly reversible, elastic regime within the tested load range. The synergistic design of the silicone encapsulation and the FBG enables near-ideal strain transfer and recovery, ensuring accuracy and repeatability under cyclic loading.

In summary, the graphical results provide multi-faceted validation of the superiority of the FBG-based flexible sensor. In terms of accuracy, it reduces systematic matching error through improved stiffness compatibility. Regarding stability, it demonstrates robustness, particularly in granular soils, where its performance is less degraded by medium heterogeneity compared to the rigid sensor. Concerning reliability, its low variance in matching coefficient and minimal hysteresis confirm excellent recoverability and promise for durable performance. These findings robustly validate the core hypothesis of this study and chart a course for developing the next generation of "soil-conformal," low-intrusive smart geotechnical sensors.

6. Conclusion

This study successfully developed and validated a novel Fiber Bragg Grating (FBG)-based flexible stress sensor, fundamentally designed to overcome the pervasive issue of soil-sensor stiffness mismatch ("matching error") inherent in conventional rigid geotechnical sensors. By encapsulating the FBG within a low-modulus silicone matrix fabricated via additive manufacturing, the sensor achieves mechanical compatibility with surrounding soil media. Comprehensive laboratory calibration and physical modeling tests in both cohesive (red clay) and granular (fine sand) soils demonstrated the sensor's superior performance. The proposed flexible sensor yielded measurements significantly closer to the theoretical Boussinesq solution than its rigid counterpart. It exhibited exceptional signal stability, particularly in granular materials where rigid sensors suffer from high variance due to the disruption of soil force chains. Furthermore, the flexible sensor showed minimal hysteresis, with its unloading curve nearly returning to the origin, confirming its operation within a highly reversible elastic regime and its reliability under cyclic loading. These results collectively affirm that the compliant design principle effectively minimizes interfacial stress disturbance, establishing a new paradigm for accurate in-situ soil stress measurement.

As a foundational investigation, this study primarily focused on sensor performance within controlled laboratory conditions and a limited elastic stress range. Future research will build upon these promising results to advance the technology toward practical field application. The immediate next step involves optimizing the sensor design, potentially through series configurations or advanced composite materials, to extend its measurable pressure range and characterize its behavior in the nonlinear, plastic deformation regime of soils. Concurrently, rigorous long-term durability tests under simulated environmental cycles (e.g., wet-dry, freeze-thaw) and high-frequency dynamic loading (simulating seismic or traffic vibration) are essential to validate its operational lifespan and stability. Finally, field trials in real geotechnical structures (e.g., embankments, retaining walls) are necessary to benchmark the sensor's performance against established monitoring methods under complex, heterogeneous field conditions. The ultimate goal is the development of scalable, distributed networks of such flexible sensors, enabling high-fidelity, real-time mapping of stress fields within geotechnical systems for improved safety and design.

7. Declarations

7.1. Author Contributions

Conceptualization, G.B. and L.Y.; methodology, G.B.; software, L.Y.; validation, G.B., L.Y., and F.L.; formal analysis, F.L.; investigation, Y.L.; resources, F.L.; data curation, F.L.; writing—original draft preparation, F.L.; writing—review and editing, G.B.; visualization, L.Y.; supervision, G.B.; project administration, G.B.; funding acquisition, G.B. All authors have read and agreed to the published version of the manuscript.

7.2. Data Availability Statement

The data presented in this study are available on request from the corresponding author.

7.3. Funding

The authors appreciate the funding provided by the Fundamental Scientific Research in Universities of Jiangsu (22KJB410001).

7.4. Acknowledgments

The authors would like to thank Mr. Xinyu Gou for his help.

7.5. Conflicts of Interest

The authors declare no conflict of interest.

8. References

[1] Bi, G., Yang, S., Wu, Y., Sun, Y., Xu, H., Zhu, B., Huang, C., & Cao, S. (2023). A preliminary study of the application of the strain-self-sensing smart geogrid rib in expansive soils. Geotextiles and Geomembranes, 51(1), 275–281. doi:10.1016/j.geotexmem.2022.10.005.

[2] Hu, Q., & Li, Y. (2022). Active Soil Pressure of Unsaturated Soil under Rainfall Conditions. Advances in Civil Engineering, 2022(1). doi:10.1155/2022/7039420.

[3] Wachman, G. S., & Labuz, J. F. (2011). Soil-Structure Interaction of an Earth Pressure Cell. Journal of Geotechnical and Geoenvironmental Engineering, 137(9), 843–845. doi:10.1061/(asce)gt.1943-5606.0000501.

[4] Ren, G., Li, T., Hu, Z., & Zhang, C. (2019). Research on new FBG soil pressure sensor and its application in engineering. Optik, 185, 759–771. doi:10.1016/j.ijleo.2019.03.019.

[5] Schenato, L., Galtarossa, A., Pasuto, A., & Palmieri, L. (2020). Distributed optical fiber pressure sensors. Optical Fiber Technology, 58, 102239. doi:10.1016/j.yofte.2020.102239.

[6] Huang, X., Wang, Y., Yang, L., & Meng, X. (2026). Research on object recognition for grasping by flexible bionic manipulator based on FBG sensors and Markov transition field. Measurement Science and Technology, 37(1), 015111. doi:10.1088/1361-6501/ae2b03.

[7] Hong, C., Yuan, Y., Yang, Y., Zhang, Y., & Abro, Z. A. (2019). A simple FBG pressure sensor fabricated using fused deposition modelling process. Sensors and Actuators, A: Physical, 285, 269–274. doi:10.1016/j.sna.2018.11.024.

[8] Lu, J., Yu, Y., Qin, S., Li, M., Bian, Q., Lu, Y., Hu, X., Yang, J., Meng, Z., & Zhang, Z. (2022). High-performance temperature and pressure dual-parameter sensor based on a polymer-coated tapered optical fiber. Optics Express, 30(6), 9714. doi:10.1364/oe.452355.

[9] He, Y., Yuan, M., Li, Q., Tang, L., Yang, W., Ping, Y., He, H., & Deng, B. (2025). Feasibility Study of Mechanical Stress Wave Detection in Power Semiconductor Devices Using Bare FBG Sensors. IEEE Sensors Journal, 25(21), 39849–39857. doi:10.1109/JSEN.2025.3615108.

[10] Lin, Y. K., Hsieh, T. S., Tsai, L., Wang, S. H., & Chiang, C. C. (2016). Using three-dimensional printing technology to produce a novel optical fiber Bragg grating pressure sensor. Sensors and Materials, 28(5), 389–394. doi:10.18494/SAM.2016.1189.

[11] Reggiani Manzo, N., T. Callado, G., M.B. Cordeiro, C., & M. Vieira Jr., L. C. (2019). Embedding optical Fiber Bragg Grating (FBG) sensors in 3D printed casings. Optical Fiber Technology, 53, 102015. doi:10.1016/j.yofte.2019.102015.

[12] Schenato, L., Rong, Q., Shao, Z., Quiao, X., Pasuto, A., Galtarossa, A., & Palmieri, L. (2019). Highly Sensitive FBG Pressure Sensor Based on a 3D-Printed Transducer. Journal of Lightwave Technology, 37(18), 4784–4790. doi:10.1109/JLT.2019.2919917.

[13] Hong, C.-Y., Huang, J., CHEN, W., & Abro, Z. A. (2022). 3d Printing of a Fiber Optic Pressure Sensor. SSRN Electronic Journal. doi:10.2139/ssrn.4246667.

[14] Wei, H. Z., Xu, D. S., & Meng, Q. S. (2018). A newly designed fiber-optic based earth pressure transducer with adjustable measurement range. Sensors (Switzerland), 18(4), 932. doi:10.3390/s18040932.

[15] Hafizi, Z. M., Vorathin, E., Aizzuddin, A. M., & Lim, K. S. (2019). High-resolution fibre bragg grating (FBG) pressure transducer for low-pressure detection. International Journal of Automotive and Mechanical Engineering, 16(2), 6783–6795. doi:10.15282/ijame.16.2.2019.23.0510.

[16] Vorathin, E., Hafizi, Z. M., Ismail, N., & Loman, M. (2020). Review of high sensitivity fibre-optic pressure sensors for low pressure sensing. Optics & Laser Technology, 121, 105841. doi:10.1016/j.optlastec.2019.105841.

[17] Luo, Z., Hua, P., Xu, B., Zhang, X., Shi, Y., & Dong, H. (2023). Research on small-sized earth pressure sensor based on ultra-weak fiber Bragg grating. Optik, 280, 170780. doi:10.1016/j.ijleo.2023.170780.

[18] Duan, Y., He, S., Wu, J., Su, B., & Wang, Y. (2022). Recent Progress in Flexible Pressure Sensor Arrays. Nanomaterials, 12(14), 2495. doi:10.3390/nano12142495.

[19] Xu, F., Li, X., Shi, Y., Li, L., Wang, W., He, L., & Liu, R. (2018). Recent developments for flexible pressure sensors: A review. Micromachines, 9(11), 580. doi:10.3390/mi9110580.

[20] Dong, S., Ma, S., Zhou, T., Lou, Y., Xiong, X., Wei, K., Luo, D., Wu, J., Liu, H., Tao, R., Yang, T., & Dong, Y. (2025). A Miniaturized FBG Tactile Sensor for the Tip of a Flexible Ureteroscope. Sensors, 25(9), 2807. doi:10.3390/s25092807.

[21] Xu, D., Feng, D., Chen, Q., Liu, G., & Qiao, X. (2023). Small-sized temperature and pressure sensors based on fiber Bragg grating for oil and gas wells. Sensors and Actuators A: Physical, 357, 114397. doi:10.1016/j.sna.2023.114397.

[22] Lai, W., Duoc Nguyen, H., Liu, J., Chen, X., & Jay Phee, S. (2025). An FBG-Based Flexible Force Sensor for Stable Grasping in a Grow-and-Twine Gripping System. IEEE Sensors Journal, 25(21), 39545–39553. doi:10.1109/JSEN.2025.3612378.

[23] Defez, B., Madrigal, J., Sales, S., & Gosalbez, J. (2025). Mechanical FBG-Based Sensor for Leak Detection in Pressurized Pipes: Design, Modal Tuning, and Validation. Sensors, 25(23), 7260. doi:10.3390/s25237260.

[24] Kirby, J. M. (1999). Soil stress measurement: Part I. Transducer in a uniform stress field. Journal of Agricultural Engineering Research, 72(2), 151–160. doi:10.1006/jaer.1998.0357.

[25] Kirby, J. M. (1999). Soil stress measurement. Part 2: Transducer beneath a circular loaded area. Journal of Agricultural Engineering Research, 73(2), 141–149. doi:10.1006/jaer.1998.0400.